PNAS RESEARCH ARTICLE | BIOPHYSICS AND COMPUTATIONAL BIOLOGY

ALS mutations in the TIA-1 prion-like domain trigger highly condensed pathogenic structures

Naotaka Sekiyama[a,1], Kiyofumi Takaba[b], Saori Maki-Yonekura[b], Ken-ichi Akagi[c,2], Yasuko Ohtani[a], Kayo Imamura[a], Tsuyoshi Terakawa[a], Keitaro Yamashita[d], Daigo Inaoka[a], Koji Yonekura[b,e,f], Takashi S. Kodama[a,1,3], and Hidehito Tochio[a,1]

Edited by Robert Tycko, National Institute of Diabetes and Digestive and Kidney Diseases, Bethesda, MD; received December 16, 2021; accepted July 22, 2022

T cell intracellular antigen-1 (TIA-1) plays a central role in stress granule (SG) formation by self-assembly via the prion-like domain (PLD). In the TIA-1 PLD, amino acid mutations associated with neurodegenerative diseases, such as amyotrophic lateral sclerosis (ALS) or Welander distal myopathy (WDM), have been identified. However, how these mutations affect PLD self-assembly properties has remained elusive. In this study, we uncovered the implicit pathogenic structures caused by the mutations. NMR analysis indicated that the dynamic structures of the PLD are synergistically determined by the physicochemical properties of amino acids in units of five residues. Molecular dynamics simulations and three-dimensional electron crystallography, together with biochemical assays, revealed that the WDM mutation E384K attenuated the sticky properties, whereas the ALS mutations P362L and A381T enhanced the self-assembly by inducing β-sheet interactions and highly condensed assembly, respectively. These results suggest that the P362L and A381T mutations increase the likelihood of irreversible amyloid fibrillization after phase-separated droplet formation, and this process may lead to pathogenicity.

intrinsically disordered protein regions | liquid–liquid phase separation | neurodegenerative diseases

Significance

T cell intracellular antigen-1 (TIA-1) has been studied for two decades since the beginning of stress granule research, not only because it is a major constituent of stress granules but also because of its diverse physiological functions. In this study, we elucidated how disease-associated mutations alter the self-assembly mode at an atomic level and proposed a five-amino acid model that quantifies the sticker and spacer properties that potentially act within TIA-1 prion-like domain droplets. This model enabled us to evaluate how disease-associated mutations can exert a significant impact on the condensate properties. Our research has the potential to elucidate the molecular mechanisms of neurodegenerative diseases caused by amino acid mutations in intrinsically disordered proteins.

Membraneless organelles (MLOs) are biomolecular condensates formed by physical phenomena, such as liquid–liquid phase separation and sol−gel transitions, which regulate diverse cellular functions in space and time (1). One type of the MLOs existing in the cytoplasm is stress granules (SGs), which are involved in regulating mRNA translation (2). SGs were initially identified as cytoplasmic foci formed in response to stress, composed of polyadenylated RNA [poly(A) RNA], poly(A)-binding protein I, RNA-binding protein T cell intracellular antigen-1 (TIA-1), and its homolog TIAR (3–5). Proteomics analysis of SGs revealed constituents, such as RNA-binding proteins possessing intrinsically disordered protein regions (IDRs) (6–8). In genes encoding the RNA-binding proteins, amino acid mutations associated with neurodegenerative diseases, such as amyotrophic lateral sclerosis (ALS) and frontotemporal dementia (FTD), have been identified (9, 10). These mutations are suggested to transform the SG constituents into the aberrant aggregates accumulated in neurons (2).

IDRs in these RNA-binding proteins form reversible condensates, such as liquid-like droplets or hydrogels (1, 11). These IDRs are suggested to have multiple binding and linker regions that interact multivalently to form the large molecular networks necessary for droplet formation. This concept can be modeled as a sticker-and-spacer framework, where each residue behaves as a sticker or spacer depending on the amino acid characteristics, and their connection sequence allows the unique self-assembly properties of IDRs (12). The self-assembly of IDRs is mediated by a set of diverse interactions between multiple binding residues. For example, π–π and π–sp^2 interactions in FUS (13, 14) and cation–π and electrostatic interactions in DDX4 contribute significantly to droplet formation (15, 16). In addition, several studies have indicated the importance of hydrogen bonds (17), hydrophobic interactions (18), and backbone interactions (19). On the other hand, polar residues that connect the interacting residues modulate droplet fluidity by influencing the conformational flexibility in FUS (20).

In addition to the point-type stickers with one amino acid residue as a unit, short-motif stickers composed of multiple residues frequently appear in these IDRs. Short-motif stickers in FUS, TDP-43, and hnRNPA1 form a cross-β spine of amyloid fibrils, but they have structural features that ensure reversibility, such as a kinked conformation and stacking Asp residues, referred to as the low-complexity aromatic-rich kinked segments (LARKS) and the reversible amyloid-forming cores (RAC) (21–24). The genome-wide distribution of the short-motif stickers indicates that they are involved in crucial interactions for MLOs (21). The interaction of short-motif stickers is assumed

Author contributions: N.S. and T.S.K. designed research; N.S., T.S.K., and H.T. performed research; K.T., S.M.-Y., K.-i.A., Y.O., K.I., T.T., K. Yamashita, D.I., and K. Yonekura contributed new reagents/analytic tools; N.S., K.T., S.M.-Y., Y.O., K.I., T.T., D.I., K. Yonekura, and T.S.K. analyzed data; and N.S. and T.S.K. wrote the paper.

The authors declare no competing interest.

This article is a PNAS Direct Submission.

[1]To whom correspondence may be addressed. Email: sekiyama.naotaka.5x@kyoto-u.ac.jp, tskodama@protein.osaka-u.ac.jp, or tochio@mb.biophys.kyoto-u.ac.jp.

[2]Present address: Environmental Metabolic Analysis Research Team, RIKEN Center for Sustainable Resource Science, Kanagawa 230-0045, Japan.

[3]Present address: Institute for Protein Research, Osaka University, Osaka 565-0871, Japan.

This article contains supporting information online at http://www.pnas.org/lookup/suppl/doi:10.1073/pnas.2122523119/-/DCSupplemental.

Published September 16, 2022.

to be the initial step in the transition from droplets to amyloid fibrils because of their molecular propagation characteristics (23, 24). Indeed, hnRNPA2, which forms phase-separated droplets, turns into reversible amyloid fibrils with LARKS-like kinked segments (25). FUS forms amyloid fibrils stabilized via core formation by polar residues, and phosphorylation of the core-forming residues alters the self-assembly properties of the droplets and fibrils in a coupled manner (26). Pathogenic proteins—such as tau, prions, and amyloid-β—have steric zipper-type stickers, which can become irreversible amyloid cores by interdigitating their side chains (27, 28). These studies suggest that the structural features of short-motif stickers are essential for understanding droplet and amyloid fibril formation. However, it has remained debatable whether the IDRs in the droplets form the multiresidue interactions observed in the crystal structures.

TIA-1 was identified as an RNA-binding protein that plays a central role in SG formation by its self-assembly via the C-terminal prion-like domain (PLD) (29–31). TIA-1 has been found to accumulate in pathological aggregations in the brain tissues of mouse models of Huntington's disease and tauopathy, as well as in the brain tissues of Alzheimer's disease patients, existing in a coaggregated state with huntingtin and tau proteins (32, 33), and to form amyloid fibrils (32, 34). Genetic analysis of neurodegenerative diseases, such as familial ALS/FTD or Welander distal myopathy (WDM), revealed that the TIA-1 PLD has disease-associated mutations that promote phase separation and slow the clearance of SGs (34–36). Despite the biological and clinical relevance, the self-assembly properties of PLD and the influence of the disease-associated mutations have not been fully elucidated at a residue or an atomic level. In this study, we extracted the physicochemical properties governing the droplet formation of the PLD and uncovered the implicit pathogenic structures caused by the mutations. NMR analysis indicated that the dynamic structures of the PLD are synergistically determined by the physicochemical properties of amino acids in units of five residues, whether in the sticker or spacer parts. This result indicates that a mutation of even one amino acid residue can alter the sticker-and-spacer architecture of the PLD in a context-dependent manner. Molecular dynamics simulations and three-dimensional (3D) electron crystallography (3D ED) together with biochemical assays revealed that the WDM mutation E384K attenuated the sticky properties around the mutation site, whereas the ALS mutations P362L and A381T enhanced self-assembly by inducing β-sheet interactions and highly condensed assembly, respectively. These results suggest that the P362L and A381T mutations increase the likelihood of irreversible amyloid fibrillization after phase-separated droplet formation, and this process may lead to pathogenicity.

Results

TIA-1 PLD Forms Liquid-Like Droplets. To dissect the self-assembly property of TIA-1 at the segment level, we prepared the full-length mouse TIA-1 fused with a His-SUMO tag (FL) and the PLD domain alone (PLD). When we diluted these proteins with a neutral pH buffer, FL formed liquid-like droplets as previously reported (34), while PLD formed gel-like irreversible aggregates (Fig. 1*A*). In the course of resolving the aggregates, we found that in the presence of 1 M urea, the aggregates turned into droplets and exhibited temperature-dependent reversibility (Fig. 1*A*). These results led us to speculate that TIA-1 has hydrophilic RNA-recognition motifs and a hydrophobic PLD so that FL forms droplets with a balance between protein−solvent and protein–protein interactions. In addition, in the case of the PLD, its balance could be controlled by adjusting the solution conditions. We thus inferred that the condensate property could be manipulated by encompassing an appropriate amino acid region of the PLD. To investigate this concept, we made various deletion mutants of the PLD lacking its N terminus while leaving its C terminus because of the clustering of disease-associated mutations (34). After examining the properties of each deletion mutant, we found that the PLD lacking 30 residues in the N terminus (small PLD, smPLD) (*SI Appendix*, Fig. S1) formed temperature-dependent reversible droplets (Fig. 1 *A* and *B*). In the fluorescence recovery after photobleaching experiments, the smPLD droplets had a 28% recovery rate of fluorescence intensity after 5 min (*SI Appendix*, Fig. S2), indicating fluidity inside the droplet. This result suggests that the fluidity of the smPLD droplets is lower than that of the other phase-separated droplets, such as FUS (13), DDX4 (16), and even full-length TIA-1 (34), all of which displayed over 50% recovery within 5 min. These results suggest that TIA-1 attained reversible droplet formation by balancing protein–solvent and protein–protein interactions, and the balance can be manipulated by the solvent conditions and the amino acid sequence of the protein.

IDRs of RNA-binding proteins are responsible for their localization to SGs in cells (37–40). To validate the effect of TIA-1 PLD, we quantified the capability of SG localization in HeLa cells with full-length TIA-1 or each TIA-1 deletion mutant. In the cells expressing TIA-1 FL fused with GFP, arsenite treatment caused the formation of TIA-1^{+} SG-like puncta in the cytoplasm (*SI Appendix*, Fig. S3*A*). On the other hand, in the cells expressing TIA-1 lacking the PLD or smPLD (ΔPLD or ΔsmPLD), puncta were formed but in fewer numbers per cell than those formed in FL; in the ΔPLD and ΔsmPLD cells, the number of puncta was reduced to a similar extent (*SI Appendix*, Fig. S3*B*). This suggests that both the PLD and smPLD contribute to SG localization and that smPLD retains the full activity of the PLD.

Among the ALS/WDM mutations in the TIA-1 PLD, the residues found normally at the mutated positions of the P362L, A381T, and E384K mutants are conserved among organisms (*SI Appendix*, Fig. S1), and these mutations are shown to promote phase separation of TIA-1 and delay the clearance of SGs (34). To elucidate the mechanism by which these mutations had profound effects on TIA-1, we investigated the self-assembly properties of the WT and ALS/WDM mutants. Since the number of amino acid residues in the PLD domain is the same in mice and humans, we employed the sequence numbering of human TIA-1. ALS/WDM mutants, similar to the WT, formed temperature-dependent reversible droplets. We also found that these smPLD droplets took up thioflavin T (ThT), a reagent for detecting amyloid fibrils, and emitted strong fluorescence (Fig. 1*C*). Image analysis showed that P362L and A381T had larger droplet areas while E384K had a smaller droplet area compared to than WT, despite comparable particle sizes (*SI Appendix*, Fig. S4). Turbidity measurements of smPLD droplets showed that P362L and A381T mutations increased droplet formation compared to the WT, whereas E384K decreased droplet formation (Fig. 1*D*). To quantify the molecules incorporated into the droplet, we estimated the droplet ratio, which is the ratio between the protein amount dissolved in the supernatant and the amount precipitated in droplets, using tryptophan fluorescence. As with the image analysis and the turbidity measurement, mutants P362L and A381T incorporated more smPLD molecules than the WT, although E384K incorporated fewer (Fig. 1*E*). These results show that

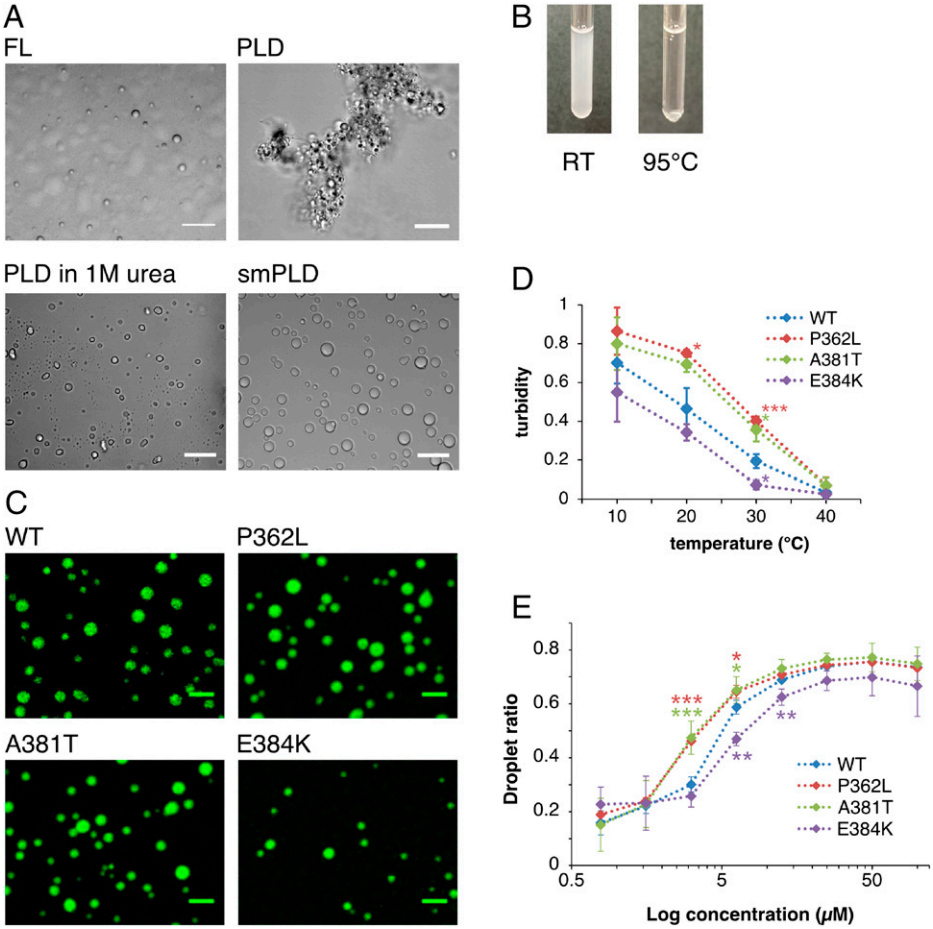

Fig. 1. TIA-1 smPLD forms temperature-dependent reversible liquid-like droplets. (*A*) Brightfield image of the droplets formed by full-length TIA-1 fused with a His-SUMO tag (FL), PLD, PLD in 1 M urea, or smPLD. Each sample was prepared at a protein concentration of 50 μM with buffer consisting of 50 mM MES, pH 6.5, 150 mM NaCl, and 1 mM DTT. (Scale bar, 10 μm.) (*B*) The temperature dependency of smPLD droplets. A test tube contains 100 μM of smPLD with the same buffer as that in *A*. The *Left* and *Right* panels show the test tube incubated at room temperature (RT) and boiling water, respectively. (*C*) Fluorescence image of WT, P362L, A381T, or E384K smPLD droplets. Each sample was prepared at a protein concentration of 10 μM with the same buffer as that in *A* supplemented with 5 μM ThT. The fluorescence image was acquired at 543 nm with excitation at 488 nm. (Scale bar, 10 μm.) (*D*) Turbidity (absorbance measured at 600 nm) at each temperature point from 10 to 40 °C. Each sample was prepared at a protein concentration of 10 μM with the same buffer as that in *A*. The experiments were recorded in triplicate. The marks represent the mean, and the error bars represent the SD. Asterisks indicate $*P < 0.05$, $**P < 0.01$, or $***P < 0.001$ by Welch's *t* test at each temperature. (*E*) Droplet ratio of WT, P362L, A381T, or E384K mutant smPLD. The measurements were performed at protein concentrations of 0.78, 1.56, 3.13, 6.25, 12.5, 25.0, 50.0, and 100 μM. Protein quantification was based on the fluorescence intensity of tryptophan (360 nm with excitation at 280 nm). Given that the intensity before centrifugation is I_{drop} and that after centrifugation is I_{sup}, the droplet ratio was calculated by $(I_{drop} - I_{sup})/I_{drop}$. The horizontal axis shows the protein concentration on a logarithmic scale. The experiments were recorded in triplicate. The marks represent the mean, and the error bars represent the SD. Asterisks indicate $*P < 0.05$, $**P < 0.01$, or $***P < 0.001$ by Welch's *t* test at each concentration.

the ALS mutations P362L and A381T promote droplet formation, but surprisingly, the WDM mutation E384K suppresses droplet formation, contrary to reports that all these mutations promote droplet formation by Mackenzie et al. (34).

We were concerned that the smPLD droplet formation inconsistency was due to truncation of TIA-1. To examine the effects of the mutations in full-length TIA-1, we prepared TIA-1 FL proteins with the P362L, A381T, or E384K mutation and performed droplet observation by microscopy, turbidity measurements, and droplet ratio experiments (*SI Appendix*, Fig. S5). These results showed that, consistent with the smPLD, P362L and A381T promoted droplet formation and E384K inhibited droplet formation compared to WT in TIA-1 FL, although there was no significant difference in the turbidity measurements between WT and A381T. We reasoned that the smPLD reflects the self-assembly properties of full-length TIA-1.

1,6-Hexanediol or Adenosine Triphosphate Dissolves smPLD Droplets. As a stepping stone to analyze the self-assembly properties of the smPLD at a residue level, we aimed to gain insights into molecular states during the dissolution process of the droplets. First, we searched for substances that could dissolve the droplets. The substances we tried were polyethylene glycol (PEG), 1,6-hexanediol (1,6-HD), and adenosine triphosphate (ATP), which are known to influence the formation of droplets, hydrogels, and SGs (30, 41–43), and potassium chloride (KCl), which affects electrostatic interactions. Turbidity measurement was of the sample containing the smPLD droplets and each substance. The results showed that 500 mM KCl or 10% PEG reduced droplet formation by 30% or 40%, while 10% 1,6-HD and 10 mM ATP completely inhibited droplet formation (Fig. 2 *A*–*C*). Since 1,6-HD has been reported to melt FUS hydrogels in vitro or SGs in cells (41, 42), these results suggest that smPLD has interaction modes that are analogous to these condensates. In addition, the fact that ATP inhibited droplet formation in the intracellular concentration range of 2 to 8 mM (44) is presumed that ATP controls SG formation driven by TIA-1 in cells, as ATP has been previously suggested to be an intracellular hydrotrope for particular condensates, such as FUS, TAF15, hnRNPA3, and PGL-3 (43).

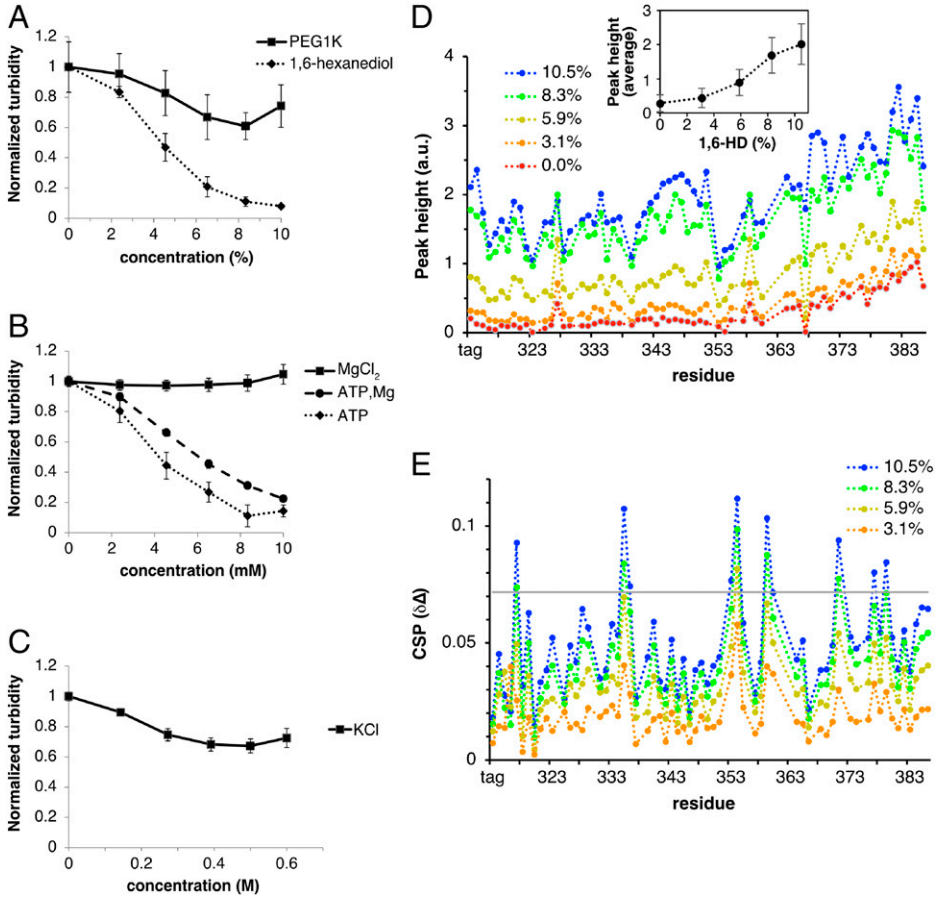

Fig. 2. 1,6-HD or ATP dissolves smPLD droplets. (*A*–*C*) Titration experiments of smPLD droplets. The horizontal axis shows the concentration of each titrant, and the vertical axis shows turbidity normalized by the value titrated with buffer. The measurement condition is at a protein concentration of 20 μM with buffer consisting of 50 mM MES, pH 6.5, 150 mM NaCl, and 1 mM DTT. Each titrant is PEG1K or 1,6-HD in *A*, $MgCl_2$, ATP-Mg, or ATP in *B*, and KCl in *C*. (*D*) ^{1}H-^{15}N HSQC peak intensity of each smPLD residue in the 1,6-HD titration. The *Inset* shows the increase rate of the average peak intensity with respect to the 1,6-HD concentration. (*E*) CSP value of each smPLD residue at each 1,6-HD concentration with respect to 0% 1,6-HD. The gray line represents the mean plus one SD of the CSP values at 10.5% 1,6-HD.

In the titration of 1,6-HD, the fluorescence polarization of tryptophan residues gradually decreased, while their peak wavelength did not exhibit significant shifts (*SI Appendix*, Fig. S6 *A* and *B*). These results indicate that the tryptophan residues in smPLD rotated faster in the presence of 1,6-HD.

For residue-level analysis, we performed NMR experiments, which can provide information on the molecular structures and dynamics of each residue. First, we performed HSQC measurements while titrating 1,6-HD or ATP into the smPLD sample, which contained both monomeric and phase-separated states. In the absence of additive, the peak intensities were weak and the sample was cloudy. However, with the addition of the additives, the peak intensities increased stepwise as opposed to the decrease in turbidity (Fig. 2*D* and *SI Appendix*, Fig. S6*C*). At 10.5% 1,6-HD or 10.5 mM ATP, the samples were less cloudy and gave sharp signals (*SI Appendix*, Fig. S7*A*). Given that an increase in NMR signal intensity can be attributed to increased dynamics and rapid conformational exchange, this result is consistent with the greater flexibility and fewer protein−protein interactions within smPLD and between the smPLD molecules. Moreover, the backbone chemical shifts in the presence of 1,6-HD showed that smPLD had no static secondary structure (*SI Appendix*, Fig. S8 *A* and *B*), which is consistent with the fact that 1,6-HD destabilizes protein structures (45). These results indicate that additive addition increased the number of NMR-visible molecules in the dispersed phase.

Focusing on residue-by-residue variation in a molecule, the signal intensity was higher in the C-terminal region than in the N-terminal region (Fig. 2*D* and *SI Appendix*, Fig. S7*B*), suggesting that the C terminus of smPLD has relatively increased dynamics and more rapid conformational exchange. In addition to the intensity enhancement, we observed chemical shift perturbations (CSPs) for a wide range of residues from the N- to C-terminal regions of smPLD (Fig. 2*E* and *SI Appendix*, Fig. S7*C*). These results indicated that 1,6-HD perturbed the local dynamic structures of smPLD; however, some parts were markedly affected, while others were not.

We compared the behavior of smPLD in response to 1,6-HD or ATP. Both spectra were very similar (*SI Appendix*, Fig. S7*A*), with a correlation coefficient of the peak intensities of 0.66 (*SI Appendix*, Fig. S7 *D*, *F*, and *G*), indicating that smPLD retained an overall disordered structure featuring a flexible C-terminal region in the presence of 1,6-HD or ATP. On the other hand, the correlation coefficient of the CSPs was 0.35 (*SI Appendix*, Fig. S7 *E*, *H*, and *I*), suggesting that 1,6-HD and ATP act in different manners to dissolve the smPLD droplets.

Dynamic Structures of smPLD Are Synergistically Determined by the Physicochemical Properties of Amino Acids. Next, we sought to analyze the local dynamic structures to investigate subtle structural or interaction mode changes due to the ALS/WDM mutations. The ^{1}H-^{15}N HSQC spectrum of each

P362L, A381T, and E384K were identical to that of WT except for the peak shifts of the residues around the mutation site in A381T and E384K (*SI Appendix*, Fig. S9), suggesting that these mutants also have an overall disordered structure that is comparable to that of WT. We subsequently measured the ^{15}N relaxation rates of backbone amide groups to probe the rotational motion of each residue (Fig. 3*A*) and found subtle differences between WT and mutants (Fig. 3*B*). The rotational correlation time τ_c, an indicator of molecular tumbling motion, was calculated from the relaxation rates to be 2.9 ns, which was comparable between WT, P362L, A381T, and E384K. This value is nearly consistent with the rotational correlation time of 3.6 ns that was estimated from the molecular weight of smPLD, indicating that smPLD exists as a monomer in the presence of 10% of 1,6-HD.

We noted that the relaxation rates of smPLD had residues with relatively higher and lower rates (Fig. 3*A*). In general, the relaxation rates of IDRs have been shown to depend on intramolecular interactions or on intermolecular interactions in the case of a condensed phase (46, 47). Based on the hypothesis that 1,6-HD competitively inhibits intermolecular interactions within the droplets, we inferred that the nonuniform relaxation rates indirectly contain information on the characteristics of the intermolecular interactions, and that the interaction modes are derived from the amino acid sequence. To verify this assumption, we performed the following analysis. First, to quantitatively evaluate the relationship between amino acid type and the relaxation rate, we assigned an index value, called an index of local dynamics (ILD), to each amino acid type and attempted to reconstruct the relaxation rates using these values. This process is based on the idea that the same type of residue contributes to the same extent to the relaxation rates. However, regardless of how we optimized the ILD values to fit the experimental values, the correlation coefficient between the predicted and the experimental values never surpassed 0.5. Therefore, assuming that the local dynamics of one residue are affected by its adjacent residues, we devised a model in which the predicted value of each residue is given the geometric mean of the ILD values of the residue and its surrounding residues. After examining various models with different regions, such as contiguous 3, 5, and 7 residues, to calculate the predicted values, we found that the geometric mean of the ILD values of the five residues consisting of the selected residue and four surrounding residues (five-amino acid model) was the best model to reproduce the experimental values (Fig. 3*C*). The sequence of steps leading to the five-amino acid model is described in *SI Appendix*, Scheme S1 and Dataset S1. The correlation coefficients between the predicted and experimental values were 0.78, 0.83, and 0.81 for R1, R2, and hNOE, respectively (Fig. 3*D*).

We next hypothesized that the ILD values obtained from the five-amino acid model represent the physicochemical properties of the amino acids, and thus compared the ILD values with 566 types of numerical indices representing the physicochemical and biochemical properties of amino acids (48, 49). As a result, the ILD values turned out to be highly correlated with certain physicochemical properties, such as partition coefficients or transfer free energy from organic solvents to water (50–52), as shown in Fig. 3*E*. These parameters describe how each amino acid distributes between nonpolar hydrophobic and polar hydrophilic environments.

The intriguing aspect of the ILD values indicates that the relaxation rates implicitly include the physicochemical properties related to the solvation of amino acids. We attributed this to the properties of 1,6-HD, which dissolves the smPLD droplets and remained at 10% during the measurements. Given that 1,6-HD forms hydrophobic interactions and hydrogen bonds with protein surfaces (45, 53), it was implied that 1,6-HD interacts nonspecifically with the protein in a manner that disrupts protein−protein interactions within the droplets. We inferred that residues with large ILD values have a large interaction surface with 1,6-HD and slow dynamics, while those with small ILD values have a small interaction surface with 1,6-HD and fast dynamics.

Second, the fact that the relaxation rate of one residue is reproduced as the geometric mean of the ILD values of five residues suggests that the local dynamic structures of smPLD are determined by the synergistic actions of multiple residues. In the above analysis, models that used fewer than five residues to calculate the predicted values had lower reproducibility of the experimental values than the five-amino acid model. Conversely, models with seven, nine, or more residues showed high reproducibility but poorer agreements between the ILD values and amino acid indices, suggesting that these models are overfitted and do not reflect the context of the smPLD amino acid sequence. These facts imply that the five-residue frame is the appropriate unit constituting the local dynamic structures.

In the relaxation rate analysis, we developed a five-amino acid model, suggesting that the five-residue frame acts synergistically to construct the local dynamic structures and that the dynamics are derived from the 1,6-HD interactions with amino acids. Given that the NMR relaxation of IDRs occurs due to the segmental motions of multiple residues associated with intramolecular interactions (54), smPLD seems to contain the five residues as a unit of the segments. In addition, considering that the 1,6-HD is an efficient competitive inhibitor of the intermolecular interactions within the droplets, we infer that the relaxation rates quantify the sticker and spacer properties potentially working within the droplets, such as high relaxation rates for stickers and low relaxation rates for spacers.

The five-amino acid model in the relaxation rate analysis implies that even one amino acid mutation can alter the local dynamic structures by affecting the immediate surroundings in a context-dependent manner. Comparison of the relaxation rates of WT with those of the mutants showed a tendency that P362L and A381T had higher relaxation rates in the adjacent regions of the mutation site, while E384K caused lower relaxation rates around the mutation site (Fig. 3*B*). These results suggest that P362L and A381T enhanced the sticker property while E384K attenuates it. This result is consistent with the biochemical assays showing that P362L and A381T promote and E384K inhibits droplet formation (Fig. 1 *D* and *E*). We surmised that the conversion of the interaction mode in P362L, A381T, and E384K could be attributed to the local dynamic structural changes in the region adjacent to the mutation site.

P362L Induces β-Sheet Interactions in Its Adjacent Region. To analyze the effects of the ALS/WDM mutations on the dynamic structures at an atomic level, we implemented all-atom molecular dynamics (MD) simulations. To enhance the structural sampling, we used the truncated peptide region encompassing the mutation sites and the residues whose relaxation rates were altered in the NMR experiments.

First, we performed MD simulations of the WT and P362L forms of region 1 (P361–P372). To compare the structural ensembles in the two trajectories, we performed principal component analysis (PCA) using backbone dihedral angles as coordinates (55). In the PCA of both the WT and P362L integrated data, the first principal component (PC1) had a 15.6% contribution and

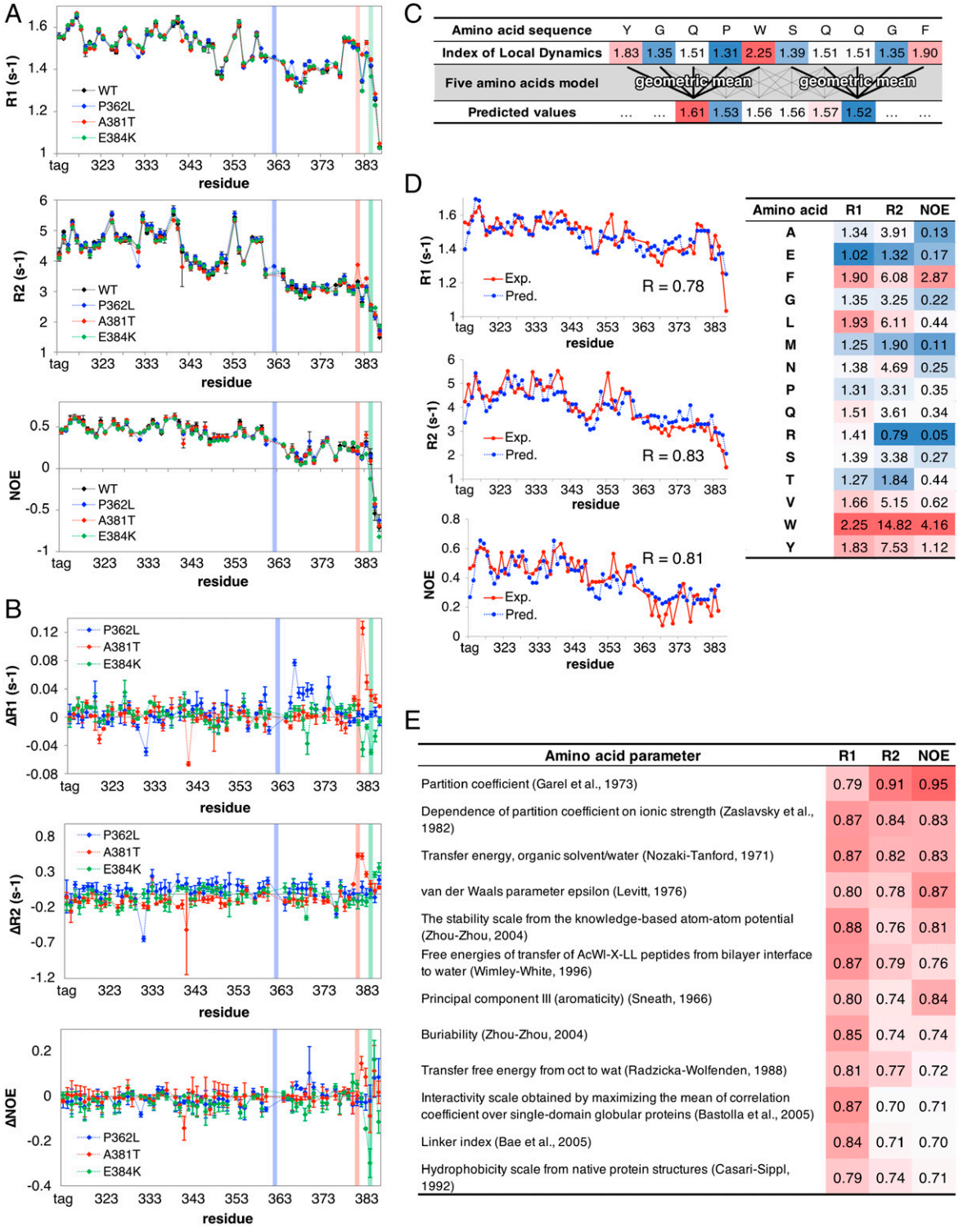

Amino acid	R1	R2	NOE
A	1.34	3.91	0.13
E	1.02	1.32	0.17
F	1.90	6.08	2.87
G	1.35	3.25	0.22
L	1.93	6.11	0.44
M	1.25	1.90	0.11
N	1.38	4.69	0.25
P	1.31	3.31	0.35
Q	1.51	3.61	0.34
R	1.41	0.79	0.05
S	1.39	3.38	0.27
T	1.27	1.84	0.44
V	1.66	5.15	0.62
W	2.25	14.82	4.16
Y	1.83	7.53	1.12

E

Amino acid parameter	R1	R2	NOE
Partition coefficient (Garel et al., 1973)	0.79	0.91	0.95
Dependence of partition coefficient on ionic strength (Zaslavsky et al., 1982)	0.87	0.84	0.83
Transfer energy, organic solvent/water (Nozaki-Tanford, 1971)	0.87	0.82	0.83
van der Waals parameter epsilon (Levitt, 1976)	0.80	0.78	0.87
The stability scale from the knowledge-based atom-atom potential (Zhou-Zhou, 2004)	0.88	0.76	0.81
Free energies of transfer of AcWl-X-LL peptides from bilayer interface to water (Wimley-White, 1996)	0.87	0.79	0.76
Principal component III (aromaticity) (Sneath, 1966)	0.80	0.74	0.84
Buriability (Zhou-Zhou, 2004)	0.85	0.74	0.74
Transfer free energy from oct to wat (Radzicka-Wolfenden, 1988)	0.81	0.77	0.72
Interactivity scale obtained by maximizing the mean of correlation coefficient over single-domain globular proteins (Bastolla et al., 2005)	0.87	0.70	0.71
Linker index (Bae et al., 2005)	0.84	0.71	0.70
Hydrophobicity scale from native protein structures (Casari-Sippl, 1992)	0.79	0.74	0.71

Fig. 3. Dynamic structures of smPLD are synergistically determined by the physicochemical properties of amino acids in units of five residues. (*A*) ^{15}N relaxation rates of the backbone amide groups in WT, P362L, A381T, and E384K of smPLD. From top to bottom, the longitudinal relaxation rate R1, the transverse relaxation rate R2, and the heteronuclear NOE are shown. The color of WT, P362L, A381T, or E384K is black, blue, red, or green, respectively. The mutation site is represented by a semitransparent vertical bar in the graph, whose color follows its solid lines. The measurement condition is at ^{13}C,^{15}N-labeled smPLD of 500 μM with buffer consisting of 50 mM MES, pH 6.5, 150 mM NaCl, 1 mM DTT, 10% 1,6-HD, 5% D_2O at 310K. (*B*) Difference in the relaxation rates between WT and P362L/A381T/E384K. The color of a solid line or a semitransparent vertical bar representing each mutation site follows the previous one. (*C*) The way to predict the relaxation rates by the five-amino acid model. An amino acid parameter, called an ILD, is given to each residue, and an ILD series is created from the sequence of smPLD. Then, a geometric mean of the ILD values of the five residues, including oneself, is calculated and used as a predicted value. The ILD values are optimized to best match the experimental values. The blue-to-red color gradient indicates low-to-high values of the index of local dynamics or the predicted values. (*D*) Comparison of the experimental values of the ^{15}N relaxation rates with the predicted values calculated from the five-amino acid model. The experimental values are shown by red solid lines, and the predicted values are shown by blue dotted lines. The correlation coefficient between the experimental values and the predicted values is shown in the graph as R. The *Right* panel shows a list of the ILD values of each amino acid type obtained from the five amino acid model. The blue-to-red color gradient indicates low-to-high values of R1, R2, or NOE. (*E*) Correlation between the ILD values and physicochemical properties of amino acids. The set of ILD values obtained from the five-amino acid model analysis was compared with the numerical indices representing the physicochemical and biochemical properties of amino acids. Amino acid parameters with correlation coefficients greater than 0.7 in R1, R2, and NOE were selected and arranged in the order of the mean values of those correlation coefficients. In the color gradient, red indicates higher values.

represented the most considerable conformational change from fully extended to a bent structure (Fig. 4 *A*–*C*). Histograms of WT or P362L projected on the PC1 axis showed that P362L had distinct populations with a PC1 value of 3.0, not found in WT (Fig. 4*A*). This fraction corresponded to the β-hairpin structures stabilized by hydrophobic interactions and hydrogen bonding between the $_{370}$MLP$_{372}$ and $_{361}$PLP$_{363}$ motifs, the latter of which includes the P362L mutation site (Fig. 4 *C*–*E* and *SI Appendix*, Fig. S10 *A* and *B*). WT retained the extended structures, presumably because the WT could not form the β-sheet interaction due to the restriction of dihedral angles in the $_{361}$PPP$_{363}$ motif (*SI Appendix*, Fig. S10 *C* and *D*). These results suggest that P362L enhances the β-sheet interaction between the N-terminal $_{361}$PLP$_{363}$ motif and the C-terminal $_{370}$MLP$_{372}$ motif. Notably, the residues contributing to the PC1 dynamics in the MD simulations consistently exhibited

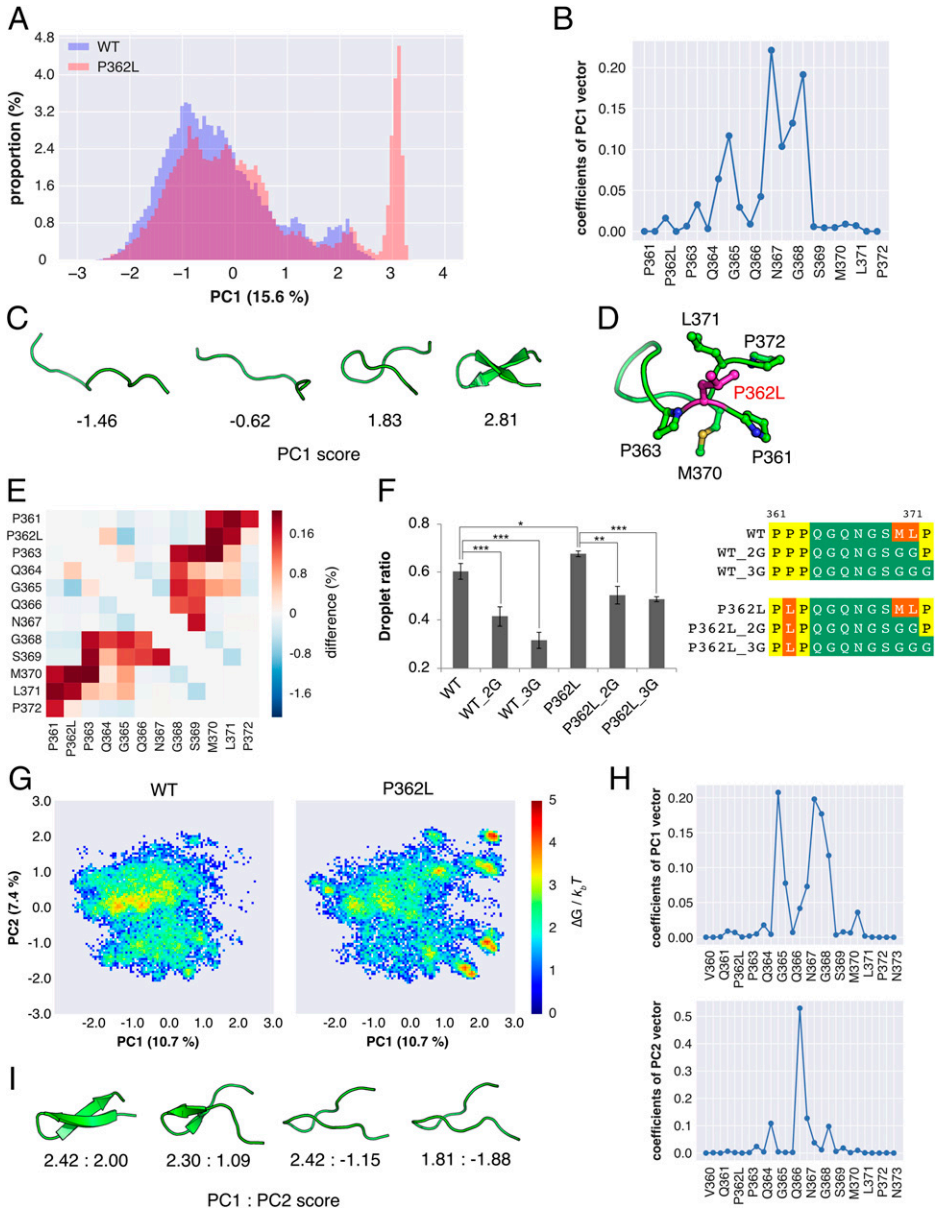

Fig. 4. P362L induces β-sheet interactions in its adjacent region. (*A*) Comparison of WT and P362L structural ensembles by the PCA analysis. The histogram shows the proportion of the structural group when the MD trajectory is projected on the PC1 component. The horizontal axis is the PC1 score, and the vertical axis is the percentage of each group with each score. WT or P362L is colored in transparent blue or red, respectively. (*B*) The coefficient of the PC1 eigenvector for each dihedral angle. The higher the coefficient value, the greater the contribution to PC1. Each residue has two plots of the φ and ψ angles in sequence, and the last P372 residue has one plot of the φ angle. (*C*) A representative structure for each PC1 score. (*D*) The β-hairpin structure observed in the P362L trajectory. The backbone and side chains are shown in a ribbon diagram and stick-and-ball models, respectively. ALS mutation site P362L is shown in magenta. (*E*) Difference map of the number of contacts between WT and P362L. The frame when Cα atoms of two residues approach within 6 Å is accounted as a contact. Here, the number of contact frames of WT is subtracted from that of P362L, and the ratio to the total frames is shown. (*F*) The droplet ratio of smPLD with a mutation in region 1. Each sample was prepared at a protein concentration of 10 μM with buffer consisting of 50 mM MES, pH 6.5, 150 mM NaCl, and 1 mM DTT. The measurements were recorded in quadruplicate. The bar represents the mean, and the error bar represents the SD. Asterisks indicate $*P < 0.05$, $**P < 0.01$, or $***P < 0.001$, by Welch's *t* test. The amino acid sequences of region 1 in smPLD mutants are shown on the right. (*G*) The free-energy landscape of hTIA-1 region 1 in WT or P362L. The histogram is based on the proportion of the structural groups obtained by projecting the MD trajectory onto the PC1 and PC2 eigenvectors of PCA. The unit is k_bT. The horizontal axis represents the score of PC1 and the vertical axis represents the score of PC2, and the contribution rates of each are shown in parentheses. (*H*) The coefficient of the PC1 or PC2 eigenvector for each dihedral angle. Each residue has two plots of the φ and ψ angles in sequence, and the last N373 residue has one plot of the φ angle. (*I*) Compact conformations representative for P362L. The PC1:PC2 scores for each structure are shown below.

different relaxation rates between WT and P362L in the NMR experiments.

In human TIA-1 (hTIA-1), P361 in mTIA-1 is replaced with Q361 (*SI Appendix*, Fig. S1). To examine this effect, we performed MD simulations using the V360-N373 region of hTIA-1 in both WT and P362L. In the case of hTIA-1 (Q361), there was more structural diversity than in mTIA-1 (P361). Thus, we compared the difference in the two-dimensional histograms PC1 and PC2 (Fig. 4*G*). The PC1 axis represented a conformational change similar to PC1 of mTIA-1, and the PC2 axis represented the motion centered on the Q366 rotation (Fig. 4*H*). The free-energy landscapes of WT and P362L suggested that WT is likely to adopt an extended conformation with a PC1 value of −2.0 to 1.0, whereas P362L is more likely to adopt a compact conformation with a PC1 value of around 2.0 (Fig. 4 *G* and *I*). P362L-specific conformations were formed by β-sheet interactions with backbone hydrogen bonding between $_{361}$QLP$_{363}$, including P362L and $_{370}$MLP$_{372}$ motifs, as observed in mTIA-1 (Fig. 4*I*). The P362L mutation expanded the potential dihedral angle distribution range of Q361 and P362L in the $_{361}$QPP$_{363}$ motif (*SI Appendix*, Fig. S11). This expansion of the dihedral angle distribution occurs in both mouse and human sequences, suggesting that P362L releases the limited backbone conformation of the $_{362}$PP$_{363}$ motif and enhances its structural multiplicity. These results also suggest that the β-sheet interaction is enhanced by P362L in hTIA-1, regardless of the P361 for Q361 substitution.

In region 1 (P361–P372) of smPLD, the WT contains abundant polar residues and had lower relaxation rates in the NMR experiments. This result indicates a substantial spacer property. In contrast, MD simulations revealed that P362L induced a sticker property in the vicinity of the mutation $_{361}$PLP$_{363}$ site and facilitated β-sheet interactions with an adjacent C-terminal sticker, $_{370}$MLP$_{372}$. From these results, we speculated that the P362L-induced sticker and its adjacent sticker could contribute to intermolecular interactions and promote droplet formation. To evaluate the effects of both stickers at once, we generated the WT and P362L 2G/3G mutant series in which the shared sticker $_{370}$MLP$_{372}$ was mutated to GGP/GGG. The droplet ratio measurements of each mutant showed that droplet formation was suppressed in both the WT and P362L 2G/3G mutant series, suggesting that the $_{370}$MLP$_{372}$ motif acts as a sticker contributing to intermolecular interactions (Fig. 4*F*). Comparison of the WT and P362L series revealed that the P362L series formed more droplets even in the 2G/3G mutant, suggesting that the P362L-induced $_{361}$PLP$_{363}$ sticker is more involved in intermolecular interactions than the $_{361}$PPP$_{363}$ motif of WT because of its conformational characteristics, as seen in MD simulations.

MD simulations revealed that the P362L-induced sticker has a strong tendency to adopt a β-sheet structure with an adjacent C-terminal sticker due to the compatibility of those side chains and the tolerance of the backbone structure. Intramolecular β-sheet interactions are transiently present in the monomer state of the prion or amyloid-β (56, 57) and are suggested to be involved as an intermediate state in amyloid fibril formation (58). Given that droplet formation concentrates protein molecules and increases molecular contacts, we infer that the two juxtaposed stickers contribute to intermolecular β-sheet interactions followed by amyloid fibril formation. In fact, droplet formation is suggested as a preliminary stage of fibrillization in α-synuclein (59). Thus, we surmise that P362L in TIA-1 accelerates irreversible aggregation via β-sheet interactions within the droplets.

We also performed MD simulations for region 2 (G377-Q386), including the A381T or E384K mutation site. In detail, A381T or E384K was more likely to adopt a slightly extended structure than the WT in terms of interactions and the radius of gyration (*SI Appendix*, Fig. S12 *C*, *D*, *G*, and *H*). However, in the PCA, there was no difference between WT and A381T or WT and E384K in the top five PC axes (*SI Appendix*, Fig. S12 *A*, *B*, *E*, and *F*), indicating that the ALS/WDM mutations did not affect the overall dynamics of region 2.

A381T Promotes Highly Condensed Assembly. To structurally clarify the effects of A381T and E384K on the self-assembly of the TIA-1 PLD, we focused on the intermolecular interactions in region 2. To this end, we attempted to crystallize region 2 peptides (G377-Q386) of the WT (R2$_{WT}$), A381T (R2$_{A381T}$), and E384K (R2$_{E384K}$). Although we could not obtain any crystals with R2$_{E384K}$, we successfully obtained tiny needle crystals with R2$_{WT}$ and R2$_{A381T}$. The crystals were too small and thin for X-ray diffraction; therefore, we collected rotational diffraction patterns using a cryoelectron microscope operated at an accelerating voltage of 300 kV. The structure of R2$_{A381T}$ was determined by the direct method using the diffraction data of R2$_{A381T}$ crystals, and the structure of R2$_{WT}$ was solved by molecular replacement using the R2$_{A381T}$ model. As a result, we built the complete model of R2$_{WT}$ and R2$_{A381T}$ with R_{work}/R_{free} = 25.98/32.54% and 27.90/34.85%, respectively (Fig. 5 *A* and *B* and *SI Appendix*, Table S1).

In both R2$_{WT}$ and R2$_{A381T}$ crystal structures, a basic unit formed by the R2 peptides was antiparallel β-sheets stabilized by the hydrophobic interactions of Y378 and V380 with Y383 and the electrostatic interaction between R379 and E384 (Fig. 5 *C* and *D*). On the other hand, their hierarchical structures assembled with the antiparallel β-sheets were completely different between WT and A381T. R2$_{WT}$ formed a triangular honeycomb structure, in which the R2 peptides were glued together by hydrogen bonding of the YR:YE motifs located at the end of the peptide and formed a trimer as a basic unit (Fig. 5 *A* and *F*). R2$_{A381T}$ stacked the β-sheets in layers, where a surface composed of A381T/Y383/T385 including the mutation site engaged in protein−protein interactions, such as hydrophobic interactions with Y383 and hydrogen bonding between A381T Oγ and Y378 Oη (Fig. 5 *B*, *G*, and *H*). The distinct hierarchical structures are attributed to the middle part of region 2 (Fig. 5*E*). The middle sequence of WT is $_{380}$VAG$_{382}$, which is exposed to the solvent in the crystal. In contrast, the corresponding region in A381T ($_{380}$VTG$_{382}$) contributes to a protein–protein interaction. These results suggest that the middle part of the R2$_{WT}$ peptide is preferentially involved in protein–solvent interactions, while the A381T mutation transforms the middle part of the R2$_{A381T}$ peptide to favor protein–protein interactions.

Next, we asked how the local interaction mode change observed in the crystal structures affects droplet formation in TIA-1 smPLD. In the droplet ratio experiments of smPLD, A381T promoted droplet formation more than WT. We reasoned that the solvation state in the middle part of region 2 might confer the difference in droplet formation between WT and A381T: droplet formation is suppressed if the middle part favors protein–solvent interactions and is promoted if the middle part stabilizes protein–protein interactions. To investigate the relevance between the crystal structures of region 2 and droplet formation, we systematically mutated the A381 residue of smPLD to hydrophilic or hydrophobic amino acids and measured the droplet ratio of each. The results showed that the droplet ratio was highly correlated with the hydrophobicity of the inserted residues at the A381 position, denoting that the increase in the sticker property in region 2 promotes the droplet formation of smPLD (Fig. 5 *I* and *J*). These results suggest

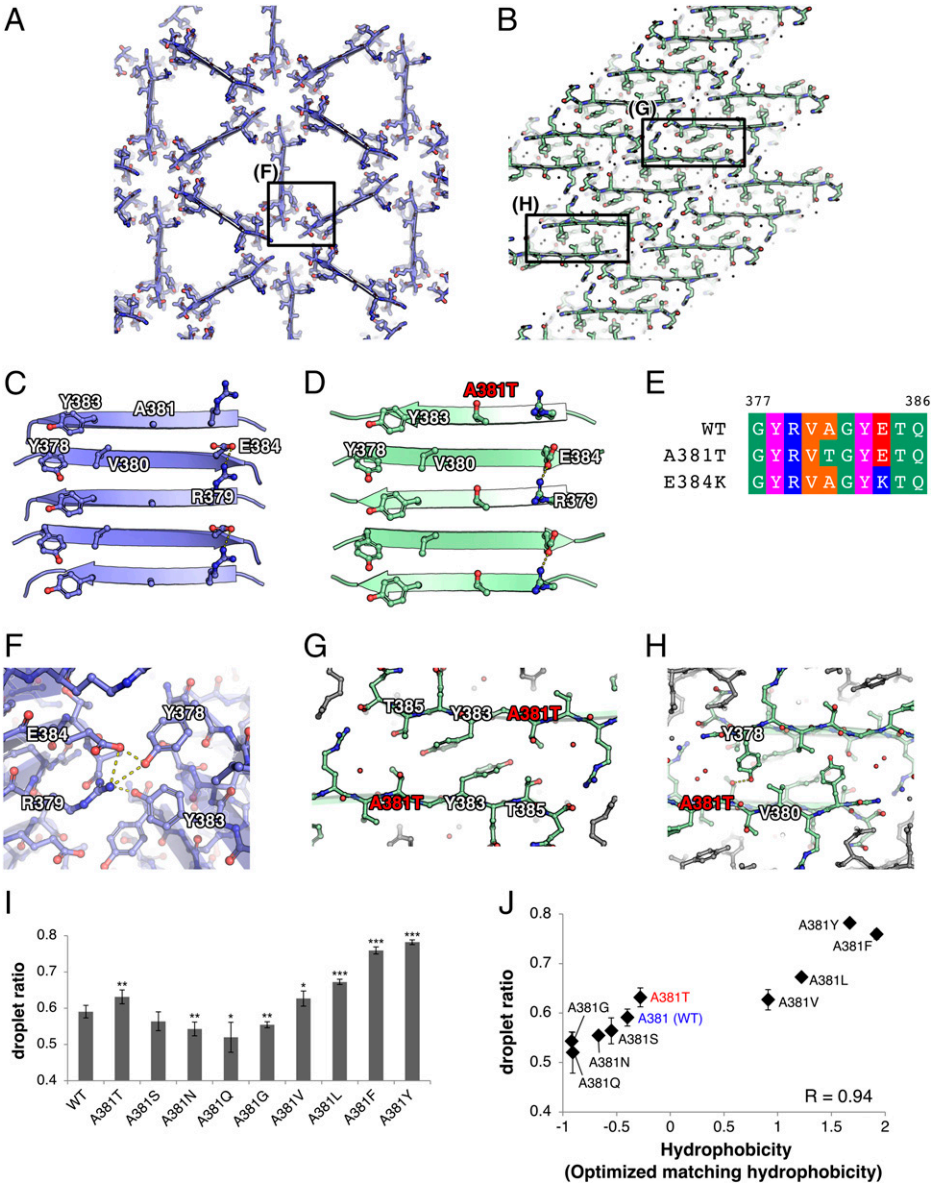

Fig. 5. A381T promotes highly condensed assembly. (*A* and *B*) Crystal structure of $R2_{WT}$ or $R2_{A381T}$ peptide. The backbone is shown as a ribbon model diagram, and the side chains are shown as stick-and-ball. $R2_{WT}$ or $R2_{A381T}$ is colored in slate or pale green, respectively. A region surrounded by the black frame is shown in *F*–*H* as an expanded view. (*C* and *D*) Antiparallel β-sheets composed of $R2_{WT}$ or $R2_{A381T}$ peptide. Both WT and A381T form identical antiparallel β-sheets, but the distinct stacking mode of these blocks has created their own hierarchical structures, such as *A* and *B*. Residue name is shown in white with a black edge, and ALS mutation, A381T, is highlighted in red. (*E*) Amino acid sequence of R2 peptides. From the top, $R2_{WT}$, $R2_{A381T}$, and $R2_{E384K}$ are shown. Polar residues such as G/T/Q are green, hydrophobic residues as V/A are orange, aromatic residues as Y are magenta, basic residues as R/K are blue, and acidic residues as in *E* are shown in red. (*F*–*H*) An interaction mode between antiparallel β-sheets. Each panel is an expanded view of the part surrounded by a black frame shown in the overall view of *A* or *B*. Dotted lines in the figure indicate hydrogen bonds, and red spheres indicate water molecules. (*I*) The droplet ratio of smPLD with a mutation at the A381 site. Each sample was prepared at a protein concentration of 10 μM with buffer consisting of 50 mM MES, pH 6.5, 150 mM NaCl, and 1 mM DTT. The measurements were recorded in quintuplicate. The bar represents the mean, and the error bar represents the SD. Asterisks indicate $*P < 0.05$, $**P < 0.01$, or $***P < 0.001$ by Welch's *t* test. (*J*) Correlation between the droplet ratio of each mutant and the hydrophobicity (optimized matching hydrophobicity) of the mutating residue. WT is shown in blue and A381T is shown in red. The correlation coefficient R is 0.94.

that A381T enhances protein–protein interactions and promotes droplet formation.

The two types of crystal structures and droplet ratio experiments clearly demonstrate the transition of a sticker property in region 2 due to A381T mutation. First, the R2 peptides of the WT formed antiparallel β-sheets; however, they were not stacked but rather preserved solvation surfaces in their assembly. These features indicate that region 2 of the WT acts as an intermediate sticker. Second, the A381T mutation increased the preference for intermolecular interaction in the crystal structure of R2 peptides. In fact, smPLD of A381T showed higher relaxation rates around the mutation site and promoted droplet formation, suggesting that A381T increased the contribution of a sticker in region 2. In addition, the R2 peptides of E384K did not produce even very small needle crystals. According to the $R2_{WT}$ and $R2_{A381T}$ crystal structures, residue E384 is an anchor point that connects the antiparallel β-sheets by an electrostatic interaction with R379, suggesting that E384K may adopt different interaction modes in region 2 from WT and A381T.

The hierarchical assembly in the crystal structures gives another indication of the condensate properties. In the two crystal structures of $R2_{WT}$ and $R2_{A381T}$, the longitudinal axis of both crystals corresponds to the direction of hydrogen bonds

forming antiparallel β-sheets (*SI Appendix*, Fig. S13). These structural features are the same principle of the cross-β structure in amyloid fibrils. However, the interaction between the side chain surfaces of the antiparallel β-sheets made a difference in the hierarchical structure of $R2_{WT}$ and $R2_{A381T}$. In $R2_{A381T}$, as shown by the extremely low solvation content of 18.36%, the peptides were packed at high density due to the face-to-face interactions between the side chain surfaces. This high-density structure is similar to the steric zipper in interdigitating the side chains, which is a hallmark of irreversible fibrils, such as tau, prion, and amyloid-β (27, 28). On the other hand, the $R2_{WT}$ peptides were sparsely packed, namely, at lower density in the crystal. $R2_{WT}$ appears to reduce the surface engaged in intermolecular interactions and minimize aggregation energy by preserving solvation surfaces. These structural features are shared with LARKS or RAC, which forms a cross-β structure while retaining the solvation surface by the kink structure and is considered to secure the reversibility of SGs or other MLOs (21, 22, 24). The solvation content of the $R2_{WT}$ crystal is 47.55%, which is at a standard level in protein crystals (60). This may also indicate that the WT sequence has no self-assembling properties that lead to irreversible amyloid fibrils, although the $R2_{WT}$ crystal exhibits distinct packing compared with the crystal structures of LARKS and RAC. From these insights, we concluded that the A381T mutation increases the frequency of protein–protein interactions in droplets and SGs and promotes the formation of highly condensed aggregates with few hydrated surfaces in the $R2_{A381T}$ crystal structure, resulting in pathogenicity.

Discussion

In this study, we investigated the molecular mechanisms governing droplet formation of the smPLD in TIA-1. The NMR analysis revealed that the relaxation rates reflecting the sticker and spacer properties were recapitulated by calculating the geometric mean of the ILD values of the five residues. The five-amino acid model implies that the sticker-and-spacer architecture is composed of not the binary attribute of each residue but rather the continuous variable properties synergistically determined by the physicochemical properties of amino acids in a unit of multiresidue frames. Our model can quantitatively consider all amino acid residues rather than specific amino acid residues and evaluate how each part of the amino acid sequence contributes to the droplet formation, whether in the sticker or spacer properties. We surmise that the quantitative sticker-and-spacer architecture serves as an example of understanding the condensate properties from the primary sequence of IDRs. It has been reported that the differences in the arrangement of aromatic residues in the IDR of hnRNPA1 are involved in determining whether the condensates become droplets or hydrogels (46). This finding suggests that aromatic residues determine the condensate properties depending on the sequence context, which is consistent with the perspective obtained in this study.

On the other hand, it is known that the relaxation rates of IDRs are dependent on conformational preferences associated with long-range intramolecular interactions (54), which may contribute to the partial discrepancy between the experimental values and the values predicted by the five-amino acid model. In addition, the TIA-1 PLD possesses few acidic and basic residues (*SI Appendix*, Fig. S1), and this bias in amino acid composition may lead to the correlation between the ILD values and solvation parameters. If the same analyses were performed on sequences that form droplets by a different mechanism from TIA-1, such as cation–π or electrostatic interactions, different parameters might be extracted.

This fragment-based approach also implies that even one amino acid mutation can produce a significant impact on its immediate surroundings in a context-dependent manner. In MD simulations and 3D electron crystallography, we showed that the ALS mutations P362L and A381T induce β-sheet interactions and highly condensed assembly, respectively. Disease-associated proline-to-leucine in other IDRs have been identified in UBQLN2 P497L for ALS (61) and hnRNPA2 P298L for Paget's disease of bone (62). These mutations transform fluid liquid-like droplets into less dynamic aggregates with changes in the NMR relaxation rates, intimating the formation of β-sheet interactions along the same lines as in TIA-1. The ALS-associated alanine-to-threonine mutation, TDP-43 A315T, forms tightly packed assemblies with a smaller solvation area than the WT peptide (24). This molecular assembly conversion is equivalent to that observed in the crystal structures of TIA-1 WT and A381T. These structural insights suggest that disease-associated mutations in IDRs often cooperate with the surrounding amino acid residues to alter the local interaction mode.

Our structural studies of TIA-1 P362L and A381T at the atomic level showed that the mutations transitioned the surrounding region to favor protein–protein interactions over protein−solvent interactions. TIA-1 has been found to accumulate in pathological aggregations in tissues from mouse models of neurodegenerative disease, as well as the brain tissues of Alzheimer's disease patients (32, 33), and to form amyloid fibrils (32, 34). These facts led us to hypothesize that the changes in the local interaction mode may affect not only droplet formation but also amyloid fibril formation. Notably, it has been reported that hnRNPA2 harbors the D290V mutation associated with ALS and multisystem proteinosis and that D290V thermodynamically stabilizes the fibrils formed by the hnRNPA2 IDR (63). Structural studies suggest that the D290V mutation does not affect the overall structural properties of the fibrils (63) but exerts a local effect that shifts the region around the mutation site from the solvent-exposed state of the WT to the protein−protein interaction state of the mutant (25). These facts suggest that even subtle changes in the local interaction mode may be inherited by the amyloid fibrils, leading to stabilization of the fibrils formed by TIA-1. Notably, however, TIA-1^{+} inclusions have not been found in tissues from ALS/FTD patients (34).

On the other hand, we found from the biochemical assays that the WDM mutation E384K suppresses droplet formation and attenuates the sticky properties in the region near the mutation site, as revealed by residue-level analysis. However, since it has been reported that E384K promotes SG formation and slows the clearance of SGs in cells (34, 35), we should distinguish the factors that influence droplet formation and SG formation.

Our structural analysis of the TIA-1 PLD illuminated the physicochemical rules that determine sticker and spacer properties in a unit of multiresidue frames and the context-dependent effects of disease-associated mutations. TIA-1 plays a central role in anchoring the interaction network in hundreds of SG constituents (6–8) and has been implied to be a key driver in forming less dynamic persistent aggregates, referred to as pathological SGs (2). These facts imply that SG constituents, including TIA-1, form reversible tangles by a precise network of molecular interactions under normal physiological conditions, while disease-associated mutations in TIA-1 and other SG constituents may fray the interaction network, resulting in pathogenic tangles with unbreakable irreversibility or laxity. However, a perspective focusing on the quantitative sticker-and-spacer architectures of

IDRs and detailed structural studies will elucidate these intricately intertwined tangles and the maturation pathway for pathological SGs.

Materials and Methods

Data Analysis with Five-Amino Acid Model. First, we assigned an ILD to each amino acid type. These values are variables that will change with subsequent analysis. Predicted values were calculated based on the ILD values. In the case of the five-amino acid model, where each amino acid is assumed to be affected by two residues on the N-terminal side and two residues on the C-terminal side, the predicted value is assigned the geometric mean of its own ILD value and the ILD values of two residues preceding the N-terminal side of itself and two residues following the C-terminal side of itself. In the final step, we optimized the ILD values to minimize the residual sum of squares between the predicted and experimental values by using the Excel Solver tool.

We compared the set of ILD values obtained from each model with the numerical indices representing physicochemical and biochemical properties of amino acids. For comparison, the amino acid parameters were standardized to have a mean of 5 and an SD of 1. We calculated the correlation coefficients between each set of ILD values and the amino acid parameters and counted the number of amino acid parameters with correlation coefficients greater than 0.7. A detailed description of all of the other methods appears in *SI Appendix*.

Complete experimental procedures including biochemical assays, MD simulations and 3D electron crystallography can be found in *SI Appendix, Supplementary Materials* and *Supplementary Methods*.

Data, Materials, and Software Availability. The atomic coordinates and structure factors have been deposited in the Protein Data Bank, https://www.wwpdb.org (PDB ID codes: 7VI4 for A381T and 7VI5 for WT) (64, 65). The backbone chemical shifts and relaxation data for TIA-1 smPLD have been deposited in BMRB (accession numbers: 51102 and 51103) (66, 67). Raw electron diffraction patterns have been deposited in Zenodo Open Data Repository (10.5281/zenodo.6921032 for A381T and 10.5281/zenodo.6923395 for WT) (68, 69) .

ACKNOWLEDGMENTS. We thank T. Yamashita and Y. Shichida for sharing the microplate reader and UV-Vis spectrophotometer; F. Ishidate for advice on microscope experiments; S. Takada for sharing computing resources; R. Suno and S. Iwata for sharing crystallization equipment; and members of the H.T. laboratory, including M. Haranosono and R. Kobayashi, for helpful discussions. Microscope experiments were performed at the iCeMS Analysis Center, Institute for Integrated Cell-Material Sciences (iCeMS), Kyoto University Institute for Advanced Study. This work was supported by the Japan Society for the Promotion of Science (JSPS) KAKENHI Grant JP19K06584 (to N.S.), Ministry of Education, Culture, Sports, Science, and Technology (MEXT) KAKENHI Grant JP22H05090 (to N.S.), JST-CREST Grant JPMJCR1762 (to H.T.), JST-Mirai Program Grant Number JPMJMI20G5 (to K. Yonekura), and the Cyclic Innovation for Clinical Empowerment from the Japan Agency for Medical Research and Development (to K. Yonekura). This work was the result of using research equipment shared in MEXT Project for promoting public utilization of advanced research infrastructure (Program for supporting introduction of the new sharing system) Grant JPMXS0421700121.

Author affiliations: [a]Department of Biophysics, Graduate School of Science, Kyoto University, Kyoto 606-8502, Japan; [b]Biostructural Mechanism Laboratory, RIKEN SPring-8 Center, Sayo 679-5148, Japan; [c]Section of Laboratory Equipment, National Institute of Biomedical Innovation, Health, and Nutrition, Osaka 567-0085, Japan; [d]Structural Studies Division, Medical Research Council Laboratory of Molecular Biology, Cambridge CB2 0QH, United Kingdom; [e]Institute of Multidisciplinary Research for Advanced Materials, Tohoku University, Sendai 980-8577, Japan; and [f]Advanced Electron Microscope Development Unit, RIKEN-JEOL Collaboration Center, RIKEN Baton Zone Program, Hyogo 679-5148, Japan

1. S. Boeynaems *et al.*, Protein phase separation: A new phase in cell biology. *Trends Cell Biol.* **28**, 420–435 (2018).
2. B. Wolozin, P. Ivanov, Stress granules and neurodegeneration. *Nat. Rev. Neurosci.* **20**, 649–666 (2019).
3. N. Kedersha, M. Gupta, W. Li, I. Miller, P. Anderson, RNA-binding proteins TIA-1 and TIAR link the phosphorylation of eIF-2alpha to the assembly of mammalian stress granules. *J. Cell Biol.* **147**, 1431–1441 (1999).
4. N. Kedersha *et al.*, Dynamic shuttling of TIA-1 accompanies the recruitment of mRNA to mammalian stress granules. *J. Cell Biol.* **151**, 1257–1268 (2000).
5. N. Kedersha *et al.*, Evidence that ternary complex (eIF2-GTP-tRNA(i)(Met))-deficient preinitiation complexes are core constituents of mammalian stress granules. *Mol. Biol. Cell* **13**, 195–210 (2002).
6. S. Jain *et al.*, ATPase-modulated stress granules contain a diverse proteome and substructure article ATPase-modulated stress granules contain a diverse proteome and substructure. *Cell* **164**, 487–498 (2016).
7. S. Markmiller *et al.*, Context-dependent and disease-specific diversity in protein interactions within stress granules. *Cell* **172**, 590–604.e13 (2018).
8. J. Y. Youn *et al.*, High-density proximity mapping reveals the subcellular organization of mRNA-associated granules and bodies. *Mol. Cell* **69**, 517–532.e11 (2018).
9. J. P. Taylor, R. H. Brown Jr., D. W. Cleveland, Decoding ALS: From genes to mechanism. *Nature* **539**, 197–206 (2016).
10. D. Ito, M. Hatano, N. Suzuki, RNA binding proteins and the pathological cascade in ALS/FTD neurodegeneration. *Sci. Transl. Med.* **9**, eaah5436 (2017).
11. M. Kato *et al.*, Cell-free formation of RNA granules: Low complexity sequence domains form dynamic fibers within hydrogels. *Cell* **149**, 753–767 (2012).
12. I. Peran, T. Mittag, Molecular structure in biomolecular condensates. *Curr. Opin. Struct. Biol.* **60**, 17–26 (2020).
13. K. A. Burke, A. M. Janke, C. L. Rhine, N. L. Fawzi, Residue-by-residue view of in vitro FUS granules that bind the C-terminal domain of RNA polymerase II. *Mol. Cell* **60**, 231–241 (2015).
14. A. C. Murthy *et al.*, Molecular interactions underlying liquid-liquid phase separation of the FUS low-complexity domain. *Nat. Struct. Mol. Biol.* **26**, 637–648 (2019).
15. J. P. Brady *et al.*, Structural and hydrodynamic properties of an intrinsically disordered region of a germ cell-specific protein on phase separation. *Proc. Natl. Acad. Sci. U.S.A.*, **114**, E8194–E8203 (2017).
16. T. J. Nott *et al.*, Phase transition of a disordered nuage protein generates environmentally responsive membraneless organelles. *Mol. Cell* **57**, 936–947 (2015).
17. B. Gabryelczyk *et al.*, Hydrogen bond guidance and aromatic stacking drive liquid-liquid phase separation of intrinsically disordered histidine-rich peptides. *Nat. Commun.* **10**, 5465 (2019).
18. C. W. Pak *et al.*, Sequence determinants of intracellular phase separation by complex coacervation of a disordered protein. *Mol. Cell* **63**, 72–85 (2016).
19. R. McCoy Vernon *et al.*, Pi-Pi contacts are an overlooked protein feature relevant to phase separation. *eLife* **7**, e31486 (2018).
20. J. Wang *et al.*, A molecular grammar governing the driving forces for phase separation of prion-like RNA binding proteins. *Cell* **174**, 688–699.e16 (2018).
21. M. P. Hughes *et al.*, Atomic structures of low-complexity protein segments reveal kinked b sheets that assemble networks. *Science*. **701**, 698–701 (2018).
22. F. Luo *et al.*, Atomic structures of FUS LC domain segments reveal bases for reversible amyloid fibril formation. *Nat. Struct. Mol. Biol.* **25**, 341–346 (2018).
23. X. Gui *et al.*, Structural basis for reversible amyloids of hnRNPA1 elucidates their role in stress granule assembly. *Nat. Commun.* **10**, 2006 (2019).
24. E. L. Guenther *et al.*, Atomic structures of TDP-43 LCD segments and insights into reversible or pathogenic aggregation. *Nat. Struct. Mol. Biol.* **25**, 463–471 (2018).
25. J. Lu *et al.*, CryoEM structure of the low-complexity domain of hnRNPA2 and its conversion to pathogenic amyloid. *Nat. Commun.* **11**, 4090 (2020).
26. D. T. Murray *et al.*, Structure of FUS protein fibrils and its relevance to self-assembly and phase separation of low-complexity domains. *Cell* **171**, 615–627.e16 (2017).
27. R. Nelson *et al.*, Structure of the cross-β spine of amyloid-like fibrils. *Nature* **435**, 773–778 (2005).
28. M. R. Sawaya *et al.*, Atomic structures of amyloid cross-β spines reveal varied steric zippers. *Nature* **447**, 453–457 (2007).
29. X. Li, J. B. Rayman, E. R. Kandel, I. L. Derkatch, Functional role of Tia1/Pub1 and Sup35 prion domains: Directing protein synthesis machinery to the tubulin cytoskeleton. *Mol. Cell* **55**, 305–318 (2014).
30. J. B. Rayman, K. A. Karl, E. R. Kandel, TIA-1 self-multimerization, phase separation, and recruitment into stress granules are dynamically regulated by Zn^2. *Cell Rep.* **22**, 59–71 (2018).
31. N. Gilks *et al.*, Stress granule assembly is mediated by prion-like aggregation of TIA-1. *Mol. Biol. Cell* **15**, 5383–5398 (2004).
32. Y. Furukawa, K. Kaneko, G. Matsumoto, M. Kurosawa, N. Nukina, Cross-seeding fibrillation of Q/N-rich proteins offers new pathomechanism of polyglutamine diseases. *J. Neurosci.* **29**, 5153–5162 (2009).
33. T. Vanderweyde *et al.*, Contrasting pathology of the stress granule proteins TIA-1 and G3BP in tauopathies. *J. Neurosci.* **32**, 8270–8283 (2012).
34. I. R. Mackenzie *et al.*, TIA1 mutations in amyotrophic lateral sclerosis and frontotemporal dementia promote phase separation and alter stress granule dynamics. *Neuron* **95**, 808–816.e9 (2017).
35. P. Hackman *et al.*, Welander distal myopathy is caused by a mutation in the RNA-binding protein TIA1. *Ann. Neurol.* **73**, 500–509 (2013).
36. J. Klar *et al.*, Welander distal myopathy caused by an ancient founder mutation in TIA1 associated with perturbed splicing. *Hum. Mutat.* **34**, 572–577 (2013).
37. D. W. Sanders *et al.*, Competing protein-RNA interaction networks control multiphase intracellular organization. *Cell* **181**, 306–324.e28 (2020).
38. J. Guillén-Boixet *et al.*, RNA-induced conformational switching and clustering of G3BP drive stress granule assembly by condensation. *Cell* **181**, 346–361.e17 (2020).
39. P. Yang *et al.*, G3BP1 is a tunable switch that triggers phase separation to assemble stress granules. *Cell* **181**, 325–345.e28 (2020).
40. D. S. W. Protter *et al.*, Intrinsically disordered regions can contribute promiscuous interactions to RNP granule assembly. *Cell Rep.* **22**, 1401–1412 (2018).
41. Y. Lin *et al.*, Toxic PR poly-dipeptides encoded by the C9orf72 repeat expansion target LC domain polymers. *Cell* **167**, 789–802.e12 (2016).
42. S. Kroschwald *et al.*, Promiscuous interactions and protein disaggregases determine the material state of stress-inducible RNP granules. *eLife* **4**, e06807 (2015).
43. A. Patel *et al.*, ATP as a biological hydrotrope. *Science* **356**, 753–756 (2017).
44. T. W. Traut, Physiological concentrations of purines and pyrimidines. *Mol. Cell. Biochem.* **140**, 1–22 (1994).

45. R. Düster, I. H. Kaltheuner, M. Schmitz, M. Geyer, 1,6-Hexanediol, commonly used to dissolve liquid-liquid phase separated condensates, directly impairs kinase and phosphatase activities. *J. Biol. Chem.* **296**, 100260 (2021).
46. E. W. Martin *et al.*, Valence and patterning of aromatic residues determine the phase behavior of prion-like domains. *Science* **367**, 694–699 (2020).
47. T. H. Kim *et al.*, Interaction hot spots for phase separation revealed by NMR studies of a CAPRIN1 condensed phase. *Proc. Natl. Acad. Sci. U.S.A.* **118**, e2104897118 (2021).
48. S. Kawashima, H. Ogata, M. Kanehisa, AAindex: Amino acid index database. *Nucleic Acids Res.* **27**, 368–369 (1999).
49. S. Kawashima, M. Kanehisa, AAindex: Amino acid index database. *Nucleic Acids Res.* **28**, 374 (2000).
50. J. P. Garel, D. Filliol, P. Mandel, Coefficients de partage d'aminoacids, nucléobases, nucléosides et nucléotide dans un système solvant salin. *J. Chromatogr. A* **78**, 381–391 (1973).
51. A. Radzicka, R. Wolfenden, Comparing the polarities of the amino acids: Side-chain distribution coefficients between the vapor phase, cyclohexane, 1-octanol, and neutral aqueous solution. *Biochemistry* **27**, 1664–1670 (1988).
52. Y. Nozaki, C. Tanford, The solubility of amino acids and two glycine peptides in aqueous ethanol and dioxane solutions. Establishment of a hydrophobicity scale. *J. Biol. Chem.* **246**, 2211–2217 (1971).
53. M. Dechene, G. Wink, M. Smith, P. Swartz, C. Mattos, Multiple solvent crystal structures of ribonuclease A: An assessment of the method. *Proteins* **76**, 861–881 (2009).
54. A. R. Camacho-Zarco *et al.*, NMR provides unique insight into the functional dynamics and interactions of intrinsically disordered proteins. *Chem. Rev.* **122**, 9331–9356 (2022).
55. A. Altis, P. H. Nguyen, R. Hegger, G. Stock, Dihedral angle principal component analysis of molecular dynamics simulations. *J. Chem. Phys.* **126**, 244111 (2007).
56. A. C. Gill, B-hairpin-mediated formation of structurally distinct multimers of neurotoxic prion peptides. *PLoS One* **9**, e87354 (2014).
57. A. Abelein *et al.*, The hairpin conformation of the amyloid β peptide is an important structural motif along the aggregation pathway. Topical issue in honor of Ivano Bertini guest editors: Lucia Banci, Claudio Luchinat. *J. Biol. Inorg. Chem.* **19**, 623–634 (2014).
58. W. Hoyer, C. Grönwall, A. Jonsson, S. Ståhl, T. Härd, Stabilization of a β-hairpin in monomeric Alzheimer's amyloid-β peptide inhibits amyloid formation. *Proc. Natl. Acad. Sci. U.S.A.* **105**, 5099–5104 (2008).
59. S. Ray *et al.*, α-Synuclein aggregation nucleates through liquid-liquid phase separation. *Nat. Chem.* **12**, 705–716 (2020).
60. B. W. Matthews, Solvent content of protein crystals. *J. Mol. Biol.* **33**, 491–497 (1968).
61. T. P. Dao *et al.*, ALS-linked mutations affect UBQLN2 oligomerization and phase separation in a position- and amino acid-dependent manner. *Structure* **27**, 937–951.e5 (2019).
62. V. H. Ryan *et al.*, Mechanistic view of hnRNPA2 low-complexity domain structure, interactions, and phase separation altered by mutation and arginine methylation. *Mol. Cell* **69**, 465–479.e7 (2018).
63. D. T. Murray *et al.*, Structural characterization of the D290V mutation site in hnRNPA2 low-complexity-domain polymers. *Proc. Natl. Acad. Sci. U.S.A.* **115**, E9782–E9791 (2018).
64. N. Sekiyama *et al.*, Data from "ALS mutations in the TIA-1 prion-like domain trigger highly condensed pathogenic structures." Protein Data Bank. https://www.rcsb.org/pdb/explore/explore.do?structureID=7VI4. Deposited 24 September 2021.
65. N. Sekiyama *et al.*, Data from "ALS mutations in the TIA-1 prion-like domain trigger highly condensed pathogenic structures." Protein Data Bank. http://www.rcsb.org/pdb/explore/explore.do?structureId=7VI5. Deposited 24 September 2021.
66. N. Sekiyama *et al.*, Data from "ALS mutations in the TIA-1 prion-like domain trigger highly condensed pathogenic structures." Biological Magnetic Resonance Data Bank. https://bmrb.io/data_library/summary/index.php?bmrbId=51102. Deposited 11 August 2022.
67. N. Sekiyama *et al.*, Data from "ALS mutations in the TIA-1 prion-like domain trigger highly condensed pathogenic structures." Biological Magnetic Resonance Data Bank. https://bmrb.io/data_library/summary/index.php?bmrbId=51103. Deposited 11 August 2022.
68. K. Takaba, S. Maki-Yonekura, N. Sekiyama, K. Yonekura, "Rotational electron diffraction patterns of TIA-1 prion-like domain, A381T mutant." Zenodo. https://doi.org/10.5281/zenodo.6921032. Deposited 18 August 2022.
69. K. Takaba, S. Maki-Yonekura, N. Sekiyama, K. Yonekura, "Rotational electron diffraction patterns of TIA-1 prion-like domain, wild type." Zenodo. https://doi.org/10.5281/zenodo.6923395. Deposited 18 August 2022.